Ultraviolet plasmonic chirality from colloidal aluminum nanoparticles exhibiting charge-selective protein detection

Author(s):
McPeak, Kevin M.; van Engers, Christian D.; Bianchi, Sarah; Rossinelli, Aurelio; Poulikakos, Lisa V.; Bernard, Laetitia; Herrmann, Sarah; Kim, David K.; Burger, Sven; Blome, Mark; Jayanti, Sriharsha V.; Norris, David J.

Publication date:
2015-10-28

Permanent link:
https://doi.org/10.3929/ethz-b-000104652

Originally published in:
Advanced Materials 27(40), https://doi.org/10.1002/adma.201503493

DOI: 10.1002/(adma.201503493)
Article type: Communication

Ultraviolet Plasmonic Chirality from Colloidal Aluminum Nanoparticles Exhibiting Charge-Selective Protein Detection

Kevin M. McPeak,[1] Christian D. van Engers,[1,2] Sarah Bianchi,[3] Aurelio Rossinelli,[1] Lisa Poulikakos,[1] Laetitia Bernard,[4] Sven Herrmann,[5] David K. Kim,[1] Sven Burger,[5,6] Mark Blome,[5,6] Sriharsha V. Jayanti,[1] and David J. Norris[1,]*

[1]Optical Materials Engineering Laboratory, Department of Mechanical and Process Engineering, ETH Zurich, 8092 Zurich, Switzerland

[2]Department of Chemistry, University of Oxford, South Parks Road, Oxford OX1 3QZ, United Kingdom

[3]Department of Biology and Chemistry, Laboratory of Biomolecular Research, Paul Scherrer Institut, 5232 Villigen PSI, Switzerland

[4]Laboratory for Nanoscale Materials Science, Empa, Überlandstrasse 129, 8600 Dübendorf, Switzerland

[5]Zuse Institute Berlin, 14195 Berlin, Germany

[6]JCMwave GmbH, 14050 Berlin, Germany

*E-mail: dnorris@ethz.ch

Keywords: chiral aluminum nanoparticles; localized surface plasmon resonances; circular dichroism; ultraviolet plasmonics; protein adsorption and detection

Abstract

Chiral aluminum nanoparticles, dispersed in water, were prepared which provide strong ultraviolet plasmonic circular dichroism, high-energy superchiral near-fields, and charge-selective protein detection.

Introduction

Plasmonic metal nanoparticles exhibit large electromagnetic-field enhancements that are useful in bio-sensing, cancer therapy, and photocatalysis.[1-3] The optical properties of such nanoparticles are extremely sensitive to the specific metal, the surrounding chemical environment, and the particle shape.[4,5] If the shape is chiral, *i.e.*, not superimposable on its mirror image, strong chiral optical effects[6-8] can occur due to asymmetric local surface

plasmon resonances (LSPRs).[9,10] To explore this effect, helical nanoparticles have typically been used.[7,8] However, recently chiral nanopyramids have also been demonstrated that provide equal if not greater chiral optical effects.[6] For any of these chiral metallic nanoparticles, circular dichroism (CD), the differential extinction between left- and right-handed light, is typically used to probe the chiral optical properties. While strong CD signals have been observed from metal nanoparticles, so far they have occurred only in the visible or near-infrared regime.[10] Biomolecules typically exhibit a chiral optical response in the ultraviolet (UV). Thus, the resonant interaction between molecular and plasmonic chirality remains an unexplored area. Its study could result in enhanced bio-sensing capabilities. Furthermore, high-energy superchiral fields[11,12] [*i.e.*, fields that are more twisted than circularly polarized light (CPL)] at the metal nanoparticle surface could drive asymmetric heterogeneous photocatalysis.[13]

To obtain such fields at UV wavelengths, traditional plasmonic metals such as Au and Ag cannot be used. In contrast, aluminum, which is the most abundant metal on Earth, can provide excellent optical properties in the UV.[14-17] Despite its reactivity and rapid oxidation,[18] Al nanostructures have been shown to support strong LSPRs in this wavelength regime.[18-20] This has led to a wide variety of applications for Al plasmonics[21] including metal-enhanced fluorescence (MEF),[22-24] surface-enhanced Raman scattering (SERS),[25-27] UV optoelectronics,[28-33] and photocatalysis.[34] The synthesis of achiral (*i.e.*, containing at least one plane of symmetry) colloidal Al nanoparticles has been performed by solution-based methods.[35-41] In addition, achiral Al nanocrystals (*i.e.*, single-crystalline nanoparticles) have also been synthesized.[42] Such nanocrystals exhibit size-dependent UV and visible plasmon modes. However, chiral Al nanoparticles have not yet been demonstrated.

Here, we report the fabrication of such nanoparticles and show how they can be used to provide charge-selective protein detection. We show that an approach, previously developed to fabricate chiral Au nanoparticles,[6] can also be exploited for Al. We then electrostatically

stabilize the resulting Al nanoparticles with citrate ligands and form aqueous colloidal dipsersions at near-physiological pH conditions. These colloids not only exhibit CD spectra with resonances in both the near-UV (>250 nm) and visible wavelengths but also normalized CD intensities comparable to the highest values reported for dispersions of Au chiral nanoparticles.[6,8] Furthermore, near-field electromagnetic simulations of the nanoparticles show a 5-fold enhancement in the optical chirality (*i.e.*, how twisted the near-field electromagnetic radiation is as compared to CPL) for both UV and visible resonances. Lastly, we demonstrate protein adsorption on our Al chiral nanoparticles, which allows detection of lysozyme at concentrations as low as 7 nanomolar (nM). These results illustrate both the large electromagnetic near-fields surrounding our chiral nanoparticles in the UV as well as their ability to bind biomolecules selectively. This combination provides opportunities to explore interactions between molecular and plasmonic chirality.

To fabricate the Al nanoparticles, we started with a route recently developed to synthesize chiral Au nanopyramids.[6] In that method, the nanoparticles are formed by depositing the metal into chiral shaped etch pits, formed via anisotropic etching on a high-index off-cut Si wafer. Because Au particles adhere poorly to the native oxide in the pits they can be removed easily by template stripping.[43] For Al, which sticks more to the native oxide, the same extraction procedure proved unsuccessful. This was slightly surprising as structured and flat Al films can be template stripped from native-oxide-covered Si wafers.[14] Apparently, the high surface area of the nanoparticles required lower adhesion in the pits for efficient removal. For this, a high-quality self-assembled monolayer (SAM) of octadecyltrichlorosilane (OTS) was grown on the surface of the etch pits prior to Al deposition. Alkyl-terminated SAMs, such as OTS, are known not to react with evaporated Al.[44] We verified this with a time-of-flight secondary ion mass spectrometry (ToF-SIMS) analysis of the OTS-coated Si template and Al films after template stripping (see Figures S1 and S2 in the Supporting Information). OTS significantly lowered the adhesion between the Al nanoparticles and the

native-oxide-covered Si etch pits, allowing for near 100% yield in the extraction of the Al nanoparticles. Movie S1 in the Supporting Information shows their expected final structure.

Once the particles were successfully removed from the chiral etch pits, we followed the steps in **Figure 1** to disperse them. Figure 1a is a sketch of a chiral Al nanoparticle attached to a Ag/glue/glass stack that was used to template strip the nanoparticle from the Si template. The Ag layer was then carefully removed by wet etching, and the Al nanoparticle array was treated with UV-ozone to form a dense 3- to 5-nm-thick native oxide (Figure 1b). UV-ozone was found to improve the stability of the Al nanoparticles in water most likely because oxidation of Al in water is known to form a porous oxide.[45] The oxidized Al nanoparticles were then dispersed in dimethylformamide (DMF) with polyvinylpyrrolidone (PVP) as the steric stabilizing agent (Figure 1c). PVP is weakly bound to the native oxide on the Al nanoparticles[46] and therefore can be readily exchanged to trisodium citrate in water (Figure 1d). The carboxyl groups on the trisodium citrate electrostatically stabilize the chiral Al nanoparticles providing a negative surface charge at physiological pH conditions.[47] Nanoparticle dispersions were stable in water for up to 3 h, after which their optical spectra started to red-shift slightly, presumably due to further oxidation that increased the local index of refraction (see Figure S3).

The chiral optical properties of aqueous dispersions of Al chiral nanoparticles were measured by CD spectroscopy (**Figure 2**a). Electron micrographs of the 140-nm-diameter left- and right-handed Al nanoparticles (where left and right are arbitrarily chosen) sitting on a Ag/glue/glass stack are shown in the corresponding insets. CD spectroscopy measures the differential extinction between left and right CPL (LCPL and RCPL).[6] Figure 2a plots the data in traditional CD units, degrees of ellipticity, which equals $14.32 \cdot c \cdot l \cdot (\varepsilon_L - \varepsilon_R)$, where c is the molar concentration, l is the optical path length, and ε_L and ε_R are the extinction coefficients for LCPL and RCPL, respectively.

In contrast to chiral molecules, which exhibit circular dichroism due to the interaction of their electric and magnetic dipoles, our Al nanoparticles have peaks in their CD spectra due to asymmetric LSPRs.[9] Direct assignment of the plasmon modes leading to these peaks is extremely challenging due to both the complexity of the shape and the various excitation directions possible on a suspended nanoparticle (see below). The bisignate nature of the CD spectra arises from the complex interplay between the plasmon modes.

However, since achiral Al nanocrystals have shown LSPRs in the UV and visible regime,[42] it is not surprising that CD spectra from chiral Al nanoparticles also have peaks at UV (*e.g.*, down to 250 nm) and visible wavelengths. The fact that spectra from the corresponding left- and right-handed particles are symmetric about the x-axis suggests that the fabrication process is well under control.

To compare these chiral optical properties with other structures, the CD spectra can be normalized in terms of the *g*-factor (also called the anisotropy factor), $[2(\varepsilon_L - \varepsilon_R)/(\varepsilon_L + \varepsilon_R)]$. The Al chiral nanoparticles have a maximum *g*-factor of 2% in the visible and 1.4% in the UV (Figure 2b). These results are on par with the highest *g*-factors reported for Au chiral nanoparticles[6,8] in the visible and to our knowledge represent the first reported *g*-factor for plasmonic CD in the ultraviolet.

The *g*-factor for a randomly oriented bare Al chiral nanoparticle in water was simulated using full three-dimensional (3D) frequency-domain finite-element simulations (JCMwave). The result is shown in Figure 2c along with a cartoon of the idealized 140-nm chiral Al nanoparticle. Apart from deviations in the UV regime, which is difficult to model due to the larger impact of material, geometry, and numerical discretization uncertainties, the simulation agrees well with experiment (Figure 2b). Simulations were also performed for Al nanoparticles uniformly coated with 5 nm of Al_2O_3 (Figure S4). The calculated *g*-factor for the oxidized particles red-shifted with respect to the spectra from the bare nanoparticles due to the increase in the local index of refraction. Our simulations also showed that if we increased

(decreased) the size of our particles, the CD peak positions would shift red (blue) but otherwise the shape and magnitude of the CD spectra did not change significantly.

It is clear from both CD measurements and electromagnetic simulations that the Al chiral nanoparticles have strong chiral optical properties in the far field. However, chiral metal nanostructures can also affect the optical properties of the electromagnetic near fields. The local chirality of such near fields can be described in terms of the optical chirality density (see Equation S1 in the Supporting Information). Originally derived by Lipkin[48] in 1964, this pseudoscalar quantity points in the direction of the field propagation and describes how tightly the corresponding field lines are twisted around a central axis.[49] To analyze it for our systems, we study its time-averaged form (see Equation S2). It has been shown[12,50,51] that chiral plasmonic nanostructures have the ability to induce strongly enhanced chiral electromagnetic near fields with an optical chirality exceeding CPL. Thus, we normalize the optical chirality by its value for CPL (see Equation S3) to obtain the optical chirality enhancement (C_{enh}).[51] When $|C_{enh}|$ equals one, the optical chirality of the near field is equivalent to CPL. $|C_{enh}|$ values larger than one indicate that the near field is more twisted than CPL. The sign of C_{enh} tells us the handedness of the twist in the near field with respect to the handedness of a given CPL excitation, with positive values being the same handedness and negative values indicating an opposite twist.

Plots of the calculated C_{enh} for a 140-nm-diameter left-handed Al chiral nanoparticle at UV and visible *g*-factor resonances (β- and δ-labeled features in Figure 2c) are shown in **Figure 3**. The nanoparticle was excited with LCPL in three different directions (k_x, k_y, and k_z) to clarify how the orientation of the particle in the dispersion could affect the near-field chirality. The three nanoparticle models on the left of Figure 3 show the respective slices of the particle at which the C_{enh} was calculated. These slices were chosen as they show the highest C_{enh} in the UV for the given excitation directions. (Expanded plots of C_{enh} for additional particle slices and excitation directions at both UV and visible wavelengths are

shown in Figures S5 and S6, respectively.) Figure 3a-c show the C_{enh} in the UV (β-labeled feature in Figure 2c) and Figure 3d-f show the C_{enh} in the visible (δ-labeled feature in Figure 2c). The maximum C_{enh} occurs at the apex of the particle with both the UV (Figure 3c) and visible (Figure 3d) resonances showing a 5-fold increase in optical chirality as compared to LCPL.

We note that the sign of C_{enh} in Figure 3 must not correspond to the sign of the far-field *g*-factor in Figure 2. The *g*-factor describes the ellipticity of the field at a given wavelength. It arises from a measurement of the CD signal, where an optically active sample is excited by LCPL and RCPL and the differential extinction is recorded. Therefore, the CD signal corresponds to the difference in absorption and scattering of LCPL and RCPL. On the other hand, C_{enh} is studied for either LCPL or RCPL. Further, in simulations of C_{enh} we have found that the sign of C_{enh} can change with distance from the structure. In previous work on nanorod dimers,[52] the sign of the chiral near field could be directly related to the far-field CD. Such a system can be approximated in the dipole limit where the mechanisms giving rise to CD are similar to those in chiral molecules.[9] For more complex shapes, such as ours, the connection between far-field and near-field chirality is far less straightforward.

However, in general, it was sharp edges on our particles, not flat surfaces, that exhibited the highest C_{enh}, irrespective of the excitation wavevector. Enhancements of 3 to 4 times that of CPL were calculated for both sharp edges near the outer rim (Figure 3b,e) and opposite of the apex (Figure 3a,d). The optical chirality at sharp edges of the particle can be understood by considering Equations S1 and S2. The locations of maximum optical chirality enhancement are related to the maxima of the electric and magnetic near fields. As the fields are highly confined at the sharp edges of the particle, this can lead to a high optical chirality enhancement in their vicinity. To the best of our knowledge, this is the first time superchiral fields in the UV regime have been reported. High-energy superchiral fields could be promising for asymmetric photocatalysis.[13]

The electromagnetic near fields surrounding colloidal metal nanoparticles are extremely sensitive to their local index of refraction. This effect can be observed by monitoring the peak positions in extinction spectra before and after the addition of an adsorbate. The peaks shift in energy by an amount related to the properties of both the metal nanoparticle and the adsorbate molecule. In general, the intensity of the near-field enhancement, the proximity of the adsorbate to the particle surface, and the size of the adsorbed molecule all affect the observed energy shift. Colloidal metal nanoparticles are stabilized by either steric hindrance from long-chain surface ligands or electrostatic repulsion from charged surface groups. Long-chain ligands restrict potential adsorbates from the strongest near fields at the metal nanoparticle surface. In contrast, electrostatically stabilized particles can allow adsorbates more intimate contact with the surface and the corresponding near fields. Electrostatically stabilized nanoparticles will also be sensitive to the charge of potential adsorbates, with like charges repelling and opposite charges leading to adsorption.

To examine the sensitivity of our citrate-stabilized Al chiral nanoparticles to adsorbates, we exposed them to different proteins under near-physiological pH conditions (pH 7.2) and measured spectroscopic shifts. Such experiments are analogous to measuring the shift in standard extinction spectra from achiral metal nanoparticles when their local dielectric environment is altered by the addition of an adsorbate.[1] In our case, we could measure both extinction and CD spectra simultaneously. However, due to the presence of broad peaks, small shifts were difficult to detect in extinction spectra (Figure S7). Thus, we focused on measuring CD. Beforehand, we verified that the CD signals from the proteins alone did not interfere with those from the Al chiral nanoparticles (Figure S8).

Because our nanoparticle dispersions are electrostatically stabilized by the negatively charged carboxyl groups bound to the native-oxide-covered Al surface, the surface charge of the protein should determine its binding affinity to the nanoparticle. Proteins with more positive charge should have a higher binding affinity to the negatively charged nanoparticle

surface and result in a greater shift in the CD spectra. To test this, we prepared dilute solutions of three proteins [lysozyme, trypsin, and bovine serum albumin (BSA)] that have different isoelectric points (IEP). When the IEP of the protein is equal to the pH of the solution, the protein will have zero net charge. Proteins with IEP values above the pH will carry a positive charge, and those with IEP values below the pH will have a negative charge. **Figure 4** shows the calculated solvent-accessible electrostatic surface potential of our three proteins, where positive potentials (blue) arise from regions of positive charge, negative potentials (red) occur from areas of negative charge, and neutral potentials (white) have no net charge.

Figure 4a shows that lysozyme, with an IEP of 11.35[53] is heavily negatively charged at physiological pH. When only 7 nM of lysozyme is added to a dispersion of our citrate-capped Al chiral nanoparticles, the γ feature in the CD spectrum shifts by ~1.5 nm to longer wavelengths (Figure 4b) due to an increase in the refractive index of the local environment around the Al nanoparticle. Doubling the concentration of lysozyme to 14 nM resulted in another ~5.5 nm red-shift. Shortly after this addition, the particles aggregated, presumably due to the neutralization of the negative surface charge of the nanoparticles by the positively charged lysozyme. This aggregation also explains the decrease in the CD signal with protein addition seen in Figure 4b.

Trypsin, with an IEP of 10.1 to 10.5,[54] has the second highest IEP of the three proteins. The electrostatic potential map for trypsin at pH 7.2 is still predominantly blue (*i.e.*, positively charged) but clearly less than lysozyme (Figure 4c). Addition of 100 nM trypsin to the Al chiral nanoparticle dispersion resulted in a ~3.5 nm red-shift of the γ feature (Figure 4d). When an additional 400 nM of trypsin was added the peak red-shifted by another ~4 nm. (Again, slight aggregation of the particles caused the small decrease in the CD signal.) Thus, compared to lysozyme, much higher concentrations of trypsin were required to produce a noticeable shift in the CD spectra of our citrate-capped nanoparticles. Above 500 nM of trypsin the shift saturated, but colloidal stability was mostly maintained. While trypsin and

lysozyme are similar in size (23.2 versus 13.5 kDa, respectively), the decreased positive charge of trypsin decreases its binding affinity to the Al nanoparticles relative to lysozyme.

BSA, with an IEP of 4.9,[55] has the lowest IEP of the three proteins, resulting in a primarily negative surface charge at pH 7.2 (Figure 4e). As expected, the peak positions of the CD spectra were invariant even upon the addition of 500 nM BSA to the Al chiral nanoparticle dispersion. The only effect on the CD spectra was a slight decrease in the peak amplitude due to dilution effects. Both BSA and the Al nanoparticles are negatively charged at near-physiological pH conditions ensuring no electrostatic attraction between the two.

The results from Figure 4 verify that the PVP-to-trisodium-citrate ligand exchange (Figure 1) was effective. The efficacy of protein adsorption on the nanoparticles is also clearly affected by the charge of the protein. This can be explained by the electrostatic attraction between the negatively charged trisodium-citrate-capped Al nanoparticles and the positively charged proteins (*e.g.*, lysozyme and trypsin). Proteins with a negative charge (*e.g.*, BSA) were not attracted to the nanoparticles and therefore did not influence the peak position of the CD spectra. Demonstrating the ability to adsorb and sense low concentrations of biomolecules on the surface of the Al chiral nanoparticles is the first step in exploring the interaction between plasmonic and molecular chirality.

In summary, we have demonstrated that plasmonic chirality can be observed in the ultraviolet regime using chiral Al nanoparticles dispersed in water. CD measurements and electromagnetic simulations confirm strong far-field chiral optical effects in both the UV and visible regimes. The chiral nanoparticles have a maximum *g*-factor of 2% in the visible and 1.4% in the UV. These results are on par with the highest *g*-factors reported in the literature for dispersions of Au chiral nanoparticles.[6,8] Furthermore, to assess the chirality of the near-field radiation surrounding the particles we calculated the optical chirality (*i.e.*, how twisted the electromagnetic field is). We found a 5-fold increase in the optical chirality as compared to CPL for both UV and visible resonances. Field enhancements were primarily located at the

apex of the particle. Lastly, the sensitivity of the nanoparticles to biomolecule adsorption was characterized by exposing them to dilute concentrations of proteins with different surface charges under near-physiological pH conditions. Protein adsorption was monitored through shifts in the CD spectra. Lysozyme, with its strong positive surface charge, could be detected at concentrations as low as 7 nM. Therefore, the fabricated Al chiral nanoparticles exhibit strong chiral optical properties in the UV and allow biomolecules intimate contact with the chiral near field through electrostatic adsorption. They provide an ideal system to explore the interaction between molecular and plasmonic chirality within the same energy regime.

Experimental Section

Fabrication of Chiral Etch Pits in Si Templates: A previously published procedure was followed.[6] In brief, polished single-crystalline Si wafers oriented in the [137] and [-137] directions were used (Siltronix). 50 nm of SiN_x was deposited on the wafers by plasma-enhanced chemical vapor deposition (PECVD) using an Oxford Instruments PECVD 80+. The wafer was then diced into 20 x 25 mm^2 rectangles using a Disco DAD 321 wafer- and ceramic-dicing saw. Nanosphere lithography and dry plasma etching was used to fabricate a 438-nm-pitch by 160-nm-diameter hole-array mask in the SiN_x layer. Chiral etch pits were then formed in the Si templates by anisotropic wet etching in a 30 wt% aqueous KOH solution at 60 °C for approximately 1 min. The KOH solution was ultrasonicated at 40 kHz.

Self-Assembled Monolayer Formation on Si Templates: High-quality octadecyltrichlorosilane (OTS) self-assembled monolayers (SAM) were grown on our Si templates following a known protocol.[56] Octadecyltrichlorosilane (96%, Merck KGaA), bicyclohexyl (99%, Sigma-Aldrich), carbon tetrachloride (Sigma-Aldrich), and chloroform (Sigma-Aldrich) were used for OTS SAM formation and cleaning.

Metal Deposition: Thermal evaporation of Al (Kurt J. Lesker Company, 99.99%) and Ag (Kurt J. Lesker Company, 99.99%) was performed in a Kurt J. Lesker Nano 36 with the wafer

fixed normal to the incident flux. 50 nm of Al was evaporated on the OTS-coated Si templates at ~150 Å/s and a base pressure of $1x10^{-6}$ Torr or lower. A high Al deposition rate was used to avoid *in situ* oxidation of the Al and maximize its optical properties.[14] After Al evaporation, the metal deposited on the flat portions of the SiN_x layer (*i.e.* not in the Si pits) was removed using Scotch adhesive tape. Then, 180 nm of Ag (Kurt J. Lesker Company, 99.999%) was thermally evaporated on the templates at a rate of 5.0 Å/s.

Template Stripping: Template stripping was performed as previously described[6] except for the substitution of UV-cyanoacrylate glue (Loctite 4305). The glue was cured with a 365 nm Hg UV lamp for 1 hr. After curing, template stripping was performed with a razor blade.

Protein Preparation and Surface-Map Calculations: Crystalline powder of lysozyme (lysozyme from hen egg white, 62971, Sigma-Aldrich) was re-suspended directly before use to a final stock concentration of 0.038 mg/ml (2.7 μM) in 0.1 mg/ml (0.39 mM) trisodium citrate buffer. BSA (quick start bovine serum albumin standard, #500-0206, Bio-Rad Laboratories AG) was used at 2 mg/ml (30 μM) as received. Trypsin powder (from porcine pancreas, T4799, Sigma-Aldrich) was diluted directly before use to a final stock concentration of 1.5 mg/ml (54 μM) in 150 mM NaCl, 20 mM tris-(hydroxymethyl)-aminomethane hydrochloride pH=7.5 (tris-HCL), and 2 mM dithiothreitol (DTT). Solvent-accessible surfaces of lysozyme [RCSB Protein Data Bank: 1LYZ], trypsin [1S81], and BSA [3VO3] are colored by their electrostatic potential maps calculated with DelPhi.[57] Depicted in red are negative charges, in blue positive charges, and in white neutral surface areas using a range of -2 to +2 k_BT. Final images were done using the PyMOL Molecular Graphics System (Version 1.7.4, Schrödinger, LLC).

Characterization: Time-of-flight secondary ion mass spectroscopy (ToF-SIMS) was used to characterize the molecular and elemental surface species on template-stripped Al films and OTS-coated Si wafers pre- and post-template stripping. Electron microscopy was performed

immediately after template stripping using a field-emission Hitachi S-4800 scanning electron microscope (SEM) operated at an accelerating voltage of 5 kV and emission currents between 10 and 15 μA. CD spectra were collected using a Chirascan™-plus CD spectrometer (Applied Photophysics). To eliminate solvent and cuvette effects, a background CD spectrum was acquired with only the solvent prior to measuring the chiral dispersion. The initial background was subtracted from all spectra of the chiral dispersions, with and without proteins. For determining the *g*-factor (*i.e.*, anisotropy factor), the extinction spectra were measured immediately after the CD measurement in the same cuvette on a Varian Cary 300 UV-visible spectrophotometer. A J. A. Woollam V-VASE variable angle ellipsometer with rotating analyzer was used to determine the thickness of the native oxide layer on UV-ozone-exposed Al films.

Electromagnetic Simulations: The CD spectra, *g*-factor, and optical chirality density of the chiral Al nanoparticles were computed using the finite-element Maxwell's equation solver JCMsuite (JCMwave, Germany).

Supporting Information

Experimental methods, additional figures, and a movie that support the characterization and fabrication of the Al chiral nanoparticles. Supporting information is available from the Wiley Online Library or from the author.

Acknowledgements

This work was supported by the Swiss National Science Foundation under Award Number 200021-146747. C.D.v.E. acknowledges the Erasmus Student Mobility program for a Placement Grant. S.H. and S.B. acknowledge support by the Einstein Foundation Berlin (ECMath, projects SE6 and DT5). D.K. and S.V.J. were supported by the European Research Council under the European Union's Seventh Framework Programme (FP/2007-2013) / ERC Grant Agreement Nr. 339905 (QuaDoPS Advanced Grant).

Received: ((will be filled in by the editorial staff))
Revised: ((will be filled in by the editorial staff))
Published online: ((will be filled in by the editorial staff))

[1] A. J. Haes, R. P. Van Duyne, *J. Am. Chem. Soc.* **2002**, *124*, 10596.
[2] E. Boisselier, D. Astruc, *Chem. Soc. Rev.* **2009**, *38*, 1759.
[3] S. Mukherjee, F. Libisch, N. Large, O. Neumann, L. V. Brown, J. Cheng, J. B. Lassiter, E. A. Carter, P. Nordlander, N. J. Halas, *Nano Lett.* **2013**, *13*, 240.
[4] C. F. Bohren, D. R. Huffman, *Absorption and Scattering of Light by Small Particles*, Wiley-VCH Verlag GmbH, Weinheim **2004**, 286-324.
[5] K. L. Kelly, E. Coronado, L. L. Zhao, G. C. Schatz, *J. Phys. Chem. B* **2003**, *107*, 668.
[6] K. M. McPeak, C. D. van Engers, M. Blome, J. H. Park, S. Burger, M. A. Gosálvez, A. Faridi, Y. R. Ries, A. Sahu, D. J. Norris, *Nano Lett.* **2014**, *14*, 2934.
[7] A. G. Mark, J. G. Gibbs, T. C. Lee, P. Fischer, *Nat. Mater.* **2013**, *12*, 802.
[8] A. Kuzyk, R. Schreiber, Z. Y. Fan, G. Pardatscher, E. M. Roller, A. Hogele, F. C. Simmel, A. O. Govorov, T. Liedl, *Nature* **2012**, *483*, 311.
[9] Z. Y. Fan, A. O. Govorov, *Nano Lett.* **2012**, *12*, 3283.
[10] V. K. Valev, J. J. Baumberg, C. Sibilia, T. Verbiest, *Adv. Mater.* **2013**, *25*, 2517.
[11] Y. Q. Tang, A. E. Cohen, *Science* **2011**, *332*, 333.
[12] E. Hendry, T. Carpy, J. Johnston, M. Popland, R. V. Mikhaylovskiy, A. J. Lapthorn, S. M. Kelly, L. D. Barron, N. Gadegaard, M. Kadodwala, *Nat. Nanotechnol.* **2010**, *5*, 783.
[13] Y. Takano, J. Takahashi, T. Kaneko, K. Marumo, K. Kobayashi, *Earth. Planet. Sci. Lett.* **2007**, *254*, 106.
[14] K. M. McPeak, S. V. Jayanti, S. J. P. Kress, S. Meyer, S. Iotti, A. Rossinelli, D. J. Norris, *ACS Photonics* **2015**, *2*, 326.
[15] G. Hass, *J. Opt. Soc. Am.* **1955**, *45*, 945.
[16] A. D. Rakic, *Appl. Opt.* **1995**, *34*, 4755.
[17] H. Ehrenreich, H. R. Philipp, B. Segall, *Phys. Rev.* **1963**, *132*, 1918.
[18] C. Langhammer, M. Schwind, B. Kasemo, I. Zorić, *Nano Lett.* **2008**, *8*, 1461.
[19] Y. Ekinci, H. H. Solak, J. F. Loffler, *J. Appl. Phys.* **2008**, *104*, 083107.
[20] M. W. Knight, N. S. King, L. F. Liu, H. O. Everitt, P. Nordlander, N. J. Halas, *ACS Nano* **2014**, *8*, 834.
[21] D. Gerard, S. K. Gray, *J. Phys. D* **2015**, *48*, 184001.
[22] F. Mahdavi, S. Blair, *Plasmonics* **2010**, *5*, 169.
[23] K. Ray, M. H. Chowdhury, J. R. Lakowicz, *Anal. Chem.* **2007**, *79*, 6480.
[24] M. H. Chowdhury, K. Ray, S. K. Gray, J. Pond, J. R. Lakowicz, *Anal. Chem.* **2009**, *81*, 1397.
[25] T. Dörfer, M. Schmitt, J. Popp, *J. Raman Spectrosc.* **2007**, *38*, 1379.
[26] A. Taguchi, N. Hayazawa, K. Furusawa, H. Ishitobi, S. Kawata, *J. Raman Spectrosc.* **2009**, *40*, 1324.
[27] S. K. Jha, Z. Ahmed, M. Agio, Y. Ekinci, J. F. Löffler, *J. Am. Chem. Soc.* **2012**, *134*, 1966.
[28] N. Gao, K. Huang, J. Li, S. Li, X. Yang, J. Kang, *Sci. Rep.* **2012**, *2*, 816.
[29] Q. Zhang, G. Li, X. Liu, F. Qian, Y. Li, T. C. Sum, C. M. Lieber, Q. Xiong, *Nat. Commun.* **2014**, *5*, 4953.
[30] B. J. Lawrie, K. W. Kim, D. P. Norton, R. F. Haglund, *Nano Lett.* **2012**, *12*, 6152.
[31] K. Wu, Y. Lu, H. He, J. Huang, B. Zhao, Z. Ye, *J. Appl. Phys.* **2011**, *110*, 023510.
[32] N. P. Hylton, X. F. Li, V. Giannini, K. H. Lee, N. J. Ekins-Daukes, J. Loo, D. Vercruysse, P. Van Dorpe, H. Sodabanlu, M. Sugiyama, S. A. Maier, *Sci. Rep.* **2013**, *3*, 2874.

[33] R. Mupparapu, K. Vynck, I. Malfanti, S. Vignolini, M. Burresi, P. Scudo, R. Fusco, D. S. Wiersma, *Opt. Lett.* **2012**, *37*, 368.
[34] M. Honda, Y. Kumamoto, A. Taguchi, Y. Saito, S. Kawata, *Appl. Phys. Lett.* **2014**, *104*, 061108.
[35] S. W. Chung, E. A. Guliants, C. E. Bunker, D. W. Hammerstroem, Y. Deng, M. A. Burgers, P. A. Jelliss, S. W. Buckner, *Langmuir* **2009**, *25*, 8883.
[36] A. Shahravan, T. Desai, T. Matsoukas, *ACS Appl. Mater. Interfaces* **2014**, *6*, 7942.
[37] N. Arora, B. R. Jagirdar, *J. Mater. Chem.* **2012**, *22*, 9058.
[38] R. J. Jouet, A. D. Warren, D. M. Rosenberg, V. J. Bellitto, K. Park, M. R. Zachariah, *Chem. Mater.* **2005**, *17*, 2987.
[39] W. K. Lewis, A. T. Rosenberger, J. R. Gord, C. A. Crouse, B. A. Harruff, K. A. S. Fernando, M. J. Smith, D. K. Phelps, J. E. Spowart, E. A. Guliants, C. E. Bunker, *J. Phys. Chem. C* **2010**, *114*, 6377.
[40] M. J. Meziani, C. E. Bunker, F. Lu, H. Li, W. Wang, E. A. Guliants, R. A. Quinn, Y.-P. Sun, *ACS Appl. Mater. Interfaces* **2009**, *1*, 703.
[41] K. A. S. Fernando, M. J. Smith, B. A. Harruff, W. K. Lewis, E. A. Guliants, C. E. Bunker, *J. Phys. Chem. C* **2009**, *113*, 500.
[42] M. J. McClain, A. E. Schlather, E. Ringe, N. S. King, L. Liu, A. Manjavacas, M. W. Knight, I. Kumar, K. H. Whitmire, H. O. Everitt, P. Nordlander, N. J. Halas, *Nano Lett.* **2015**, *15*, 2751.
[43] P. Nagpal, N. C. Lindquist, S.-H. Oh, D. J. Norris, *Science* **2009**, *325*, 594.
[44] D. R. Jung, A. W. Czanderna, *Crit. Rev. Solid State Mater. Sci.* **1994**, *19*, 1.
[45] C. C. Chang, D. B. Fraser, M. J. Grieco, T. T. Sheng, S. E. Haszko, R. E. Kerwin, R. B. Marcus, A. K. Sinha, *J. Electrochem. Soc.* **1978**, *125*, 787.
[46] K. Ishiduki, K. Esumi, *J. Colloid Interface Sci.* **1997**, *185*, 274.
[47] F. Meder, T. Daberkow, L. Treccani, M. Wilhelm, M. Schowalter, A. Rosenauer, L. Mädler, K. Rezwan, *Acta Biomater.* **2012**, *8*, 1221.
[48] D. M. Lipkin, *J. Math. Phys.* **1964**, *5*, 696.
[49] Y. Tang, A. E. Cohen, *Phys. Rev. Lett.* **2010**, *104*, 163901.
[50] M. Schäferling, X. Yin, N. Engheta, H. Giessen, *ACS Photonics* **2014**, *1*, 530.
[51] M. Schäferling, D. Dregely, M. Hentschel, H. Giessen, *Phys. Rev. X* **2012**, *2*, 031010.
[52] N. Meinzer, E. Hendry, W. L. Barnes, *Phys. Rev. B* **2013**, *88*, 041407.
[53] L. R. Wetter, H. F. Deutsch, *J. Biol. Chem.* **1951**, *192*, 237.
[54] J. H. Northrop, *J. Gen. Physiol.* **1924**, *6*, 337.
[55] P. G. Righetti, T. Caravaggio, *J. Chromatogr. A* **1976**, *127*, 1.
[56] M. Lessel, O. Bäumchen, M. Klos, H. Hähl, R. Fetzer, M. Paulus, R. Seemann, K. Jacobs, *Surf. Interface Anal.* **2015**, *47*, 557.
[57] W. Rocchia, S. Sridharan, A. Nicholls, E. Alexov, A. Chiabrera, B. Honig, *J. Comput. Chem.* **2002**, *23*, 128.

Figures

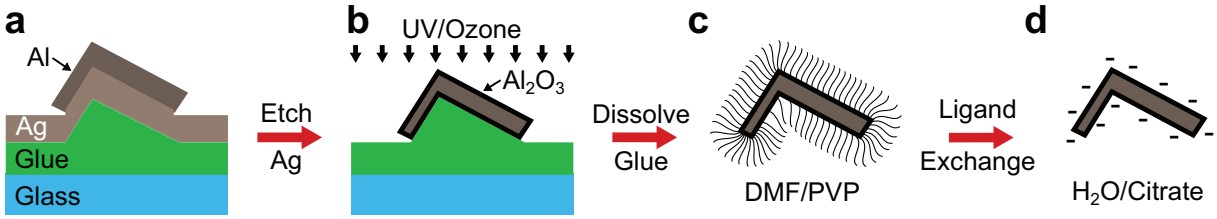

Figure 1. Schematic for the transfer of Al nanoparticles from a surface to an aqueous trisodium-citrate-stabilized colloid. (a) Al nanoparticles sitting on top of a Ag/glue/glass stack after template stripping. (b) Etching of the Ag layer and subsequent oxidation of the Al nanoparticle surfaces with UV-ozone to form a dense native oxide. (c) Simultaneous release and stabilization of the nanoparticles using DMF/PVP solution. (d) Ligand exchange of weakly bound PVP to trisodium citrate in water.

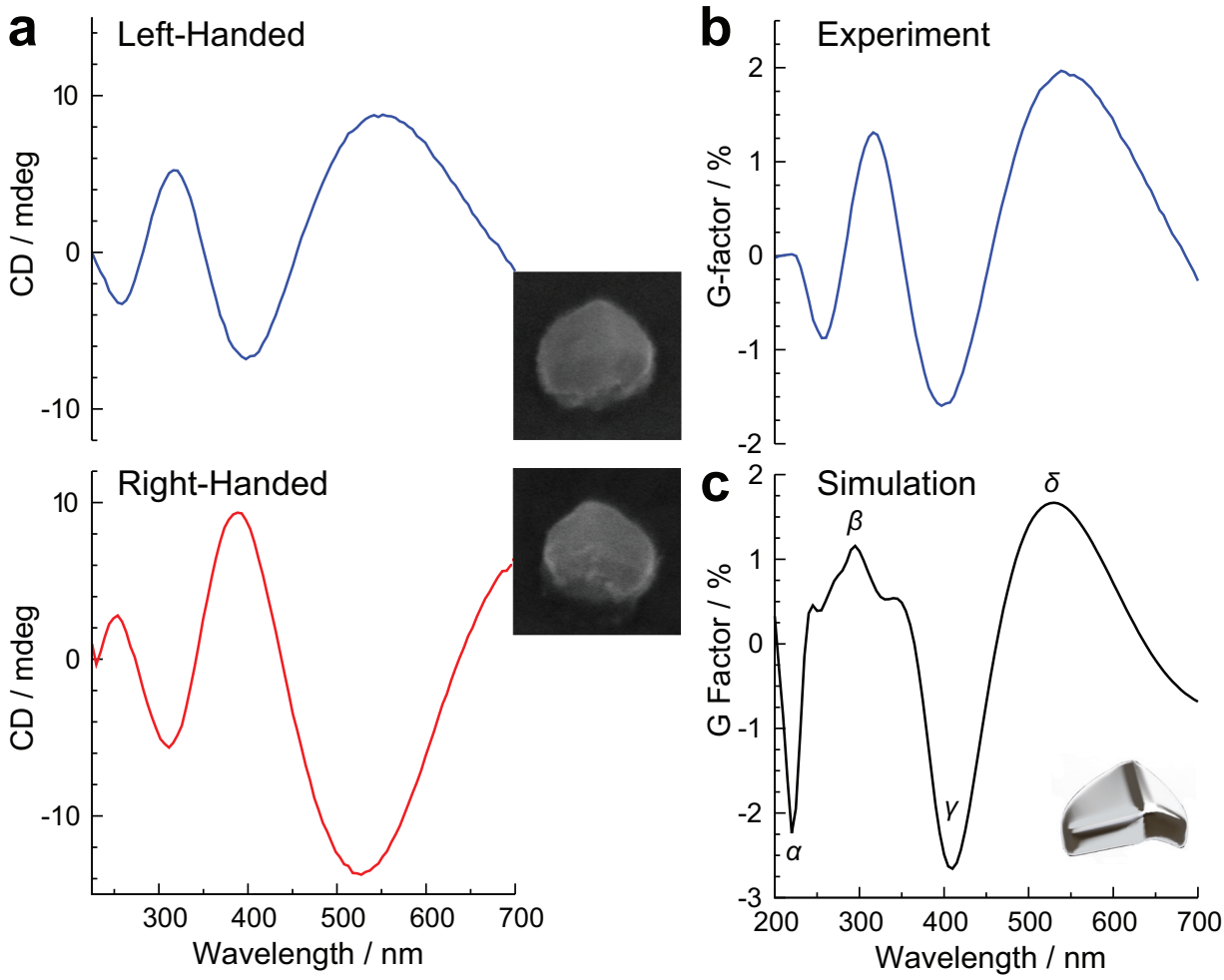

Figure 2. Measured and simulated CD spectra from Al chiral nanoparticle dispersions in water. (a) Experimental CD signals in millidegrees (mdeg) of ellipticity versus wavelength for Al nanoparticle dispersions. Left- (blue line) and right-handed (red line) pyramids (140 nm base diameter) are measured for a 2 mm path length. (Inset) Electron micrographs of left- (top) and right-handed (bottom) Al chiral nanoparticles on the Ag support film before being released by DMF. (b) Experimental CD signals versus wavelength for the left-handed nanopyramids shown in (a) plotted in terms of the *g*-factor $[2(\varepsilon_L - \varepsilon_R)/(\varepsilon_L + \varepsilon_R)]$. (c) Simulated CD spectrum (*g*-factor) for a random dispersion of idealized left-handed Al nanoparticles (inset) in water, for comparison with (b).

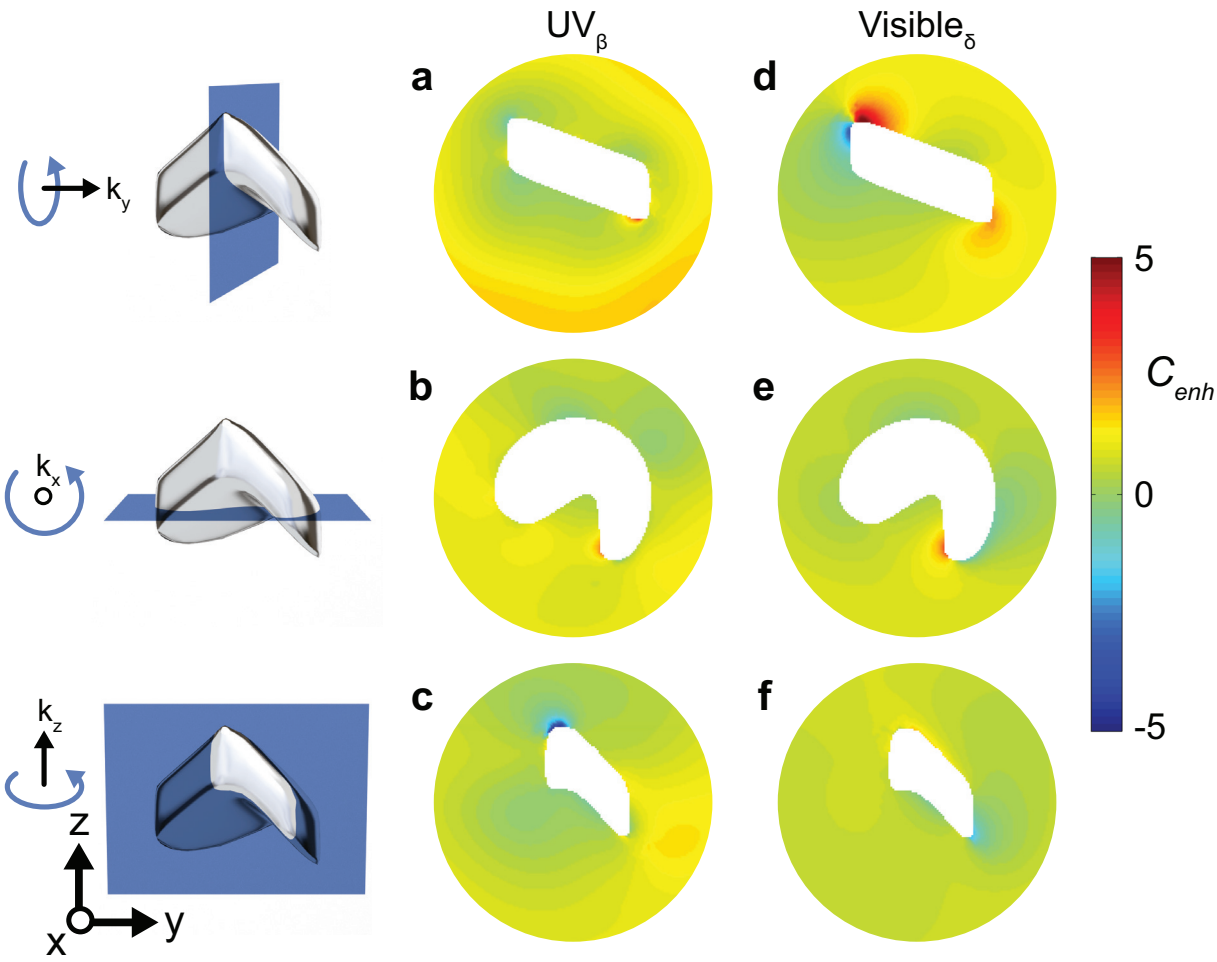

Figure 3. Calculated optical chirality enhancement (C_{enh}) for a 140-nm-diameter left-handed Al chiral nanoparticle at UV and visible *g*-factor resonances. The nanoparticle was excited with LCPL at three different wavevectors (k_x, k_y, and k_z). C_{enh} was calculated for the slices shown in the nanoparticle models on the left. (a-c) C_{enh} for various slices in the UV (β-labeled feature in Figure 2c). (d-f) C_{enh} for various slices in the visible (δ-labeled featured in Figure 2c). (a,d) C_{enh} for a slice along the ridge of the particle with k_y excitation. (b,e) C_{enh} for a slice in the XY plane at z = 0 with k_x excitation. (c,f) C_{enh} for a slice in the ZY plane at x = -50 nm with k_z excitation.

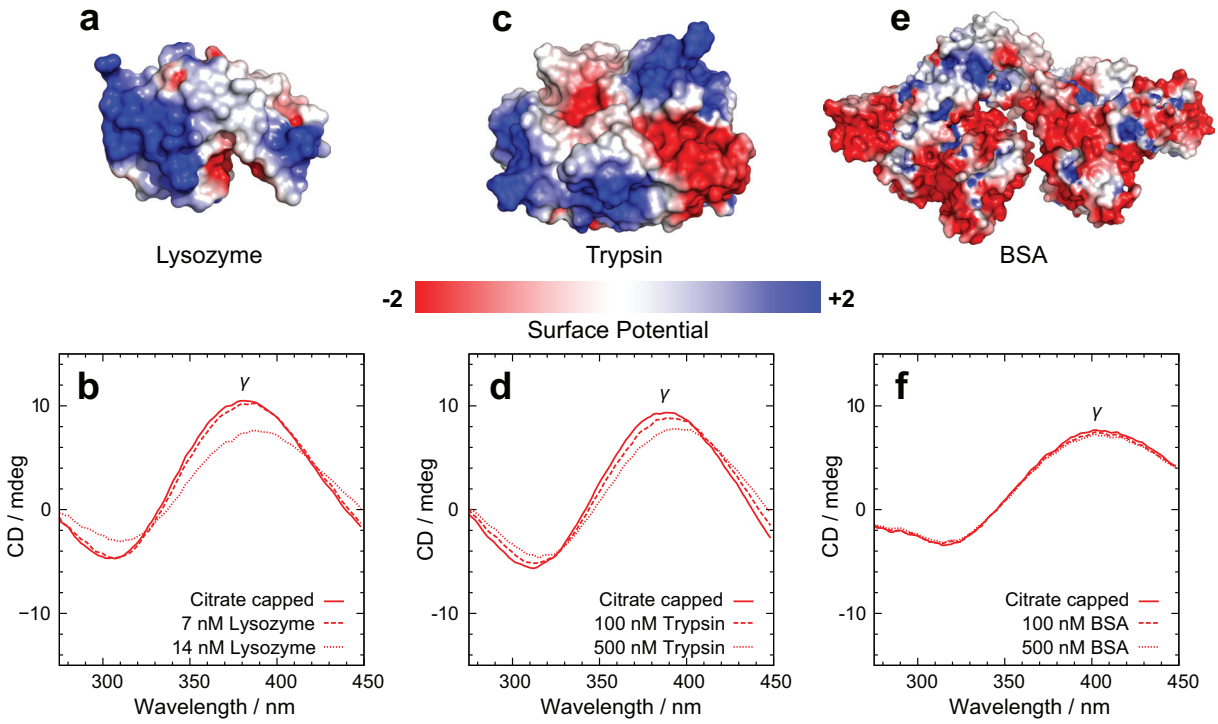

Figure 4. Calculated solvent-accessible electrostatic surface-potential maps for trypsin, lysozyme, and bovine serum albumin (BSA) at pH 7.2, with corresponding CD spectra of Al chiral nanoparticle dispersions in water before and after protein addition. (a) Electrostatic potential map for lysozyme (IEP of 11.35) showing a strong positive surface charge (red). (b) CD spectra of citrate-capped Al nanoparticle dispersions (solid) showing a ~1.5 nm red-shift in the γ feature with 7 nM lysozyme (dashed) and an additional ~5.5 nm red-shift with 14 nM lysozyme (dotted). (c) Electrostatic potential map for trypsin (IEP of 10.1 to 10.5) showing a positive surface charge (red). (d) CD spectra of citrate-capped Al nanoparticle dispersions (solid) showing a ~3.5 nm red-shift in the γ feature with 100 nM trypsin (dashed) and an additional ~4 nm red-shift with 500 nM trypsin (dotted). (e) Electrostatic potential map for BSA (IEP of 4.6) showing a negative surface charge (blue). (f) CD spectra of citrate-capped Al nanoparticle dispersions showing no peak shifts with 100 and 500 nM of BSA.

Table of contents entry:

Chiral aluminum nanoparticles, dispersed in water, were prepared which provide strong ultraviolet plasmonic circular dichroism, high-energy superchiral near-fields, and charge-selective protein detection.

Keywords: chiral aluminum nanoparticles; localized surface plasmon resonances; circular dichroism; ultraviolet plasmonics; protein adsorption and detection

Kevin M. McPeak, Christian D. van Engers, Sarah Bianchi, Aurelio Rossinelli, Lisa Poulikakos, Laetitia Bernard, Sven Hermann, David K. Kim, Mark Blome, Sven Burger, Sriharsha V. Jayanti, and David J. Norris*

Ultraviolet Plasmonic Chirality from Colloidal Aluminum Nanoparticles Exhibiting Charge-Selective Protein Detection